

See discussions, stats, and author profiles for this publication at: <https://www.researchgate.net/publication/23499483>

Kinetic Modeling of Methyl Butanoate in Shock Tube

ARTICLE in THE JOURNAL OF PHYSICAL CHEMISTRY A · DECEMBER 2008

Impact Factor: 2.69 · DOI: 10.1021/jp804358r · Source: PubMed

CITATIONS

42

READS

53

3 AUTHORS:



Lam Huynh

Vietnam National University, Ho Chi Minh ...

40 PUBLICATIONS 585 CITATIONS

SEE PROFILE



Kuang C. Lin

National Sun Yat-sen University

10 PUBLICATIONS 192 CITATIONS

SEE PROFILE



Angela Violi

University of Michigan

78 PUBLICATIONS 1,770 CITATIONS

SEE PROFILE

Article

Kinetic Modeling of Methyl Butanoate in Shock Tube

Lam K. Huynh, Kuang C. Lin, and Angela Violi

J. Phys. Chem. A, **2008**, 112 (51), 13470-13480 • DOI: 10.1021/jp804358r • Publication Date (Web): 26 November 2008

Downloaded from <http://pubs.acs.org> on January 16, 2009

More About This Article

Additional resources and features associated with this article are available within the HTML version:

- Supporting Information
- Access to high resolution figures
- Links to articles and content related to this article
- Copyright permission to reproduce figures and/or text from this article

[View the Full Text HTML](#)



ACS Publications
High quality. High impact.

The Journal of Physical Chemistry A is published by the American Chemical Society, 1155 Sixteenth Street N.W., Washington, DC 20036

Kinetic Modeling of Methyl Butanoate in Shock Tube

Lam K. Huynh, Kuang C. Lin, and Angela Violi*

Department of Mechanical Engineering, University of Michigan, Ann Arbor, Michigan 48109-2125

Received: May 16, 2008; Revised Manuscript Received: September 28, 2008

An increased necessity for energy independence and heightened concern about the effects of rising carbon dioxide levels have intensified the search for renewable fuels that could reduce our current consumption of petrol and diesel. One such fuel is biodiesel, which consists of the methyl esters of fatty acids. Methyl butanoate (MB) contains the essential chemical structure of the long-chain fatty acids and a shorter, but similar, alkyl chain. This paper reports on a detailed kinetic mechanism for MB that is assembled using theoretical approaches. Thirteen pathways that include fuel decomposition, isomerization, and propagation steps were computed using ab initio calculations [*J. Org. Chem.* **2008**, 73, 94]. Rate constants from *first principles* for important reactions in CO₂ formation, namely $\text{CH}_3\text{OCO}=\text{CH}_3 + \text{CO}_2$ (R1) and $\text{CH}_3\text{OCO}=\text{CH}_3\text{O} + \text{CO}$ (R2) reactions, are computed at high levels of theory and implemented in the mechanism. Using the G3B3 potential energy surface together with the B3LYP/6-31G(d) gradient, Hessian and geometries, the rate constants for reactions R1 and R2 are calculated using the Rice–Ramsperger–Kassel–Marcus theory with corrections from treatments for tunneling, hindered rotation, and variational effects. The calculated rate constants of reaction R1 differ from the data present in the literature by at most 20%, while those of reaction R2 are about a factor of 4 lower than the available values. The new kinetic model derived from ab initio simulations is combined with the kinetic mechanism presented by Fisher et al. [*Proc. Combust. Inst.* **2000**, 28, 1579] together with the addition of the newly found six-centered unimolecular elimination reaction that yields ethylene and methyl acetate, $\text{MB} = \text{C}_2\text{H}_4 + \text{CH}_3\text{COOCH}_3$. This latter pathway requires the inclusion of the $\text{CH}_3\text{COOCH}_3$ decomposition model suggested by Westbrook et al. [*Proc. Combust. Inst.* **2008**, accepted]. The newly composed kinetic mechanism for MB is used to study the CO₂ formation during the pyrolysis of MB as well as to investigate the autoignition of MB in a shock tube reactor at different temperatures and pressures. The computed results agree very well with experimental data present in the literature. Sensitivity and flux (rate-of-production) analyses are carried out for the CO₂ formation with the new MB mechanism, together with available reaction mechanisms, to assess the importance of various kinetic pathways for each regime. With the new mechanism, the flux analyses for the formation of C₂H species, one of the most important species for ignition delay time, are also presented at different conditions. In addition to giving a better chemical insight of the pyrolysis/oxidation of MB, the results suggest ways to improve the mechanism's capability to predict CO₂ formation and ignition delay times in pyrolysis and oxidation conditions.

1. Introduction

Biodiesel consists of the methyl esters of fatty acids, usually derived from plant oils, although other sources including animal fat are possible. Plant oils are primarily composed of different triacylglycerol molecules with three fatty acid chains (usually 18 or 16 carbons long) esterified to glycerol. The fatty acyl chains are chemically similar to the aliphatic hydrocarbons, which make up the bulk of the molecules found in petrol and diesel. Fatty acid methyl esters (FAMEs) have a formula of $\text{R}-(\text{C}=\text{O})-\text{O}-\text{CH}_3$ where R is a carbon chain of alkyl or alkenyl with as many as 16–18 carbon atoms.

Biodiesel FAMEs contain two oxygen atoms per molecule. This more oxygenated state compared to conventional diesel leads to lower carbon monoxide production and reduced emission of particulate matter.¹ In addition to containing oxygen, the FAMEs in biodiesel tend to possess one or more double bonds (depending on the triacylglycerol from which they were derived) whereas the hydrocarbons in conventional diesel are completely saturated. These double bonds strongly affect the fuel properties of biodiesel.

Biodiesel are a sustainable source of liquid transportation fuels and they are essentially neutral with respect to the production of carbon dioxide.² However, biodiesel fuels introduce new challenges for the development of reaction mechanisms. The long-chain methyl esters, while directly compatible with diesel operation, are generally difficult to study both experimentally and computationally because of their chemical complexity. In terms of kinetic mechanisms, a very large number of reactions is usually needed to model the esters.

Methyl butanoate (MB), $\text{CH}_3\text{CH}_2\text{CH}_2(\text{C}=\text{O})-\text{O}-\text{CH}_3$ (Figure 1) contains the essential chemical structure of the long-chain fatty acids, i.e., the methyl ester termination and a shorter, but similar, alkyl chain.^{3–8} In addition, detailed reaction mechanisms for MB are of a manageable size. Due to the large size of existing kinetic models for MB (usually in the order of thousands of reactions), rate constants of a significant number of elementary reactions are usually estimated from reactions available in the literature.^{3–5,7,8}

Our group has recently reported a study on potential pathways for MB breakdown using ab initio calculations. In this follow-up paper, we extend this study to develop a kinetic mechanism for MB based on reaction pathways and rates identified using

* Corresponding author. E-mail: avioli@umich.edu.

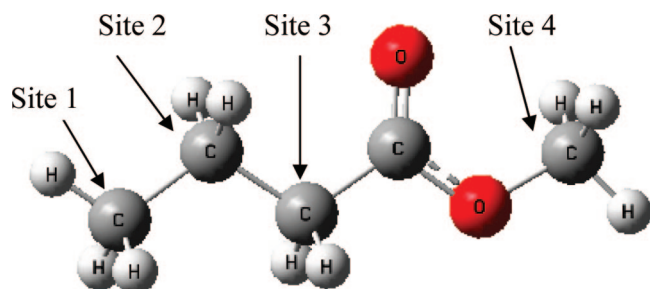


Figure 1. Structure of methyl butanoate.

TABLE 1: Barrier Heights for Hydrogen Abstraction Reactions at Different Sites of MB by Different Radicals^a

	site 1 (MB4J)	site 2 (MB3J)	site 3 (MB2J)	site 4 (MBMJ)
MB + H	8.3	6.5	6.0	8.4
MB + OH	5.0	1.9	4.1	6.2
MB + CH ₃	17.0	15.2	13.5	16.2

^a The numbers (kcal/mol) are obtained at the BH&HLYP/cc-pVTZ level of theory.

quantum chemistry and dynamics calculations.⁶ One of the main goals of this work is to obtain a kinetic mechanism to predict the formation of CO₂ in pyrolytic conditions such as shock tube experiments. Rate constants for important reactions in CO₂ formation/consumption, namely CH₃OCO=CH₃ + CO₂ (R1) and CH₃OCO=CH₃O + CO (R2) reactions, are computed using high levels of quantum mechanics and direct dynamics. The ab initio submodel is then combined with the kinetic mechanism presented by Fisher et al.³ together with the addition of the newly found six-centered unimolecular elimination reaction that yields ethylene and methyl acetate (CH₃COOCH₃),^{5,9} and the methyl acetate decomposition model.¹⁰ The newly composed kinetic model is then used to simulate the formation of carbon dioxide¹¹ and ignition delay time⁸ in shock tube experiments using MB as fuel.

2. Kinetic Model

Our group has recently reported results on reaction pathways for the breakdown of MB using quantum mechanics calculations.⁶ Electronic structures and structure-related molecular properties of reactants, intermediates, products (e.g., CO and CO₂), and transition states were explored at the BH&HLYP/cc-pVTZ level of theory. These results are used as initial data to develop a MB mechanism that can predict CO₂ in pyrolysis conditions as well as autoignition characteristics of the fuel.

2.1. Fuel Decomposition Steps. Rate constants for reactions involving hydrogen abstraction from MB by reactive flame radicals such as H, OH, and CH₃ were calculated using the transition state theory (TST) and the BH&HLYP/cc-pVTZ level of theory. These bimolecular reactions show very low barrier heights when compared with unimolecular reactions, either simple (one bond breaking at a time) or complex (multiple bonds breaking and forming at the same time) fission. For example, H abstraction from MB by H atoms has an average reaction barrier at different sites (with the zero-point energy correction) of ~7 kcal/mol at the BH&HLYP/cc-pVTZ level⁶ while the lowest barrier for the unimolecular decomposition is about 70 kcal/mol.⁹

The barrier heights for hydrogen abstraction reactions at a specific site depend on the type of attacking radicals. Table 1 reports the comparison between the energy barriers for the reactions of MB with H, OH, and CH₃ to form four MB radicals,

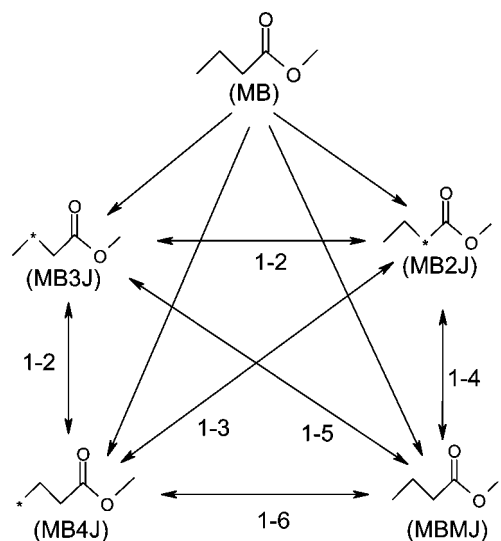


Figure 2. Isomerization reactions between initial MB radicals (MBMJ, MB2J, MB3J, and MB4J). “1-*x*” denotes the 1-*x* hydrogen migration reaction. Abbreviations used by Fisher et al.⁴ for MB radicals are given in parentheses.

TABLE 2: Barrier Heights for the Isomerization Reactions at the BH&HLYP/cc-pVTZ Level of Theory

type of migration reaction	reaction	barrier height (kcal/mol)
1-2	MB4J → MB3J	35.4
1-3	MB4J → MB2J	32.6
1-6	MB4J → MBMJ	22.5

MB3J, MB2J, MB4J, and MBMJ. The sketchy structures of these radicals are reported in Figure 2. The barrier heights for hydrogen abstraction reactions with OH and H (about 4.3 and 7.3 kcal/mol at the BH&HLYP/cc-pVTZ level of theory, respectively) are considerably lower than those for reactions by the CH₃ radicals (the averaged value of 15.5 kcal/mol). In addition, for the same reacting radical, the barrier height values depend on the site of the abstraction but the difference is not significant. The reactions at the terminal carbons (-CH₃ group) have higher barriers (3 kcal/mol) than those at nonterminal carbon (-CH₂- group).

2.2. Isomerization Steps. The four initial MB radicals (cf. Figure 2) can undergo hydrogen isomerization. These reactions are responsible for the distribution of MB radicals that are important in the propagation steps through β -scission reactions. The energy barriers depend on the type of hydrogen migration, namely 1-2, 1-3, 1-4, 1-5 and/or 1-6 hydrogen migration reactions (see Figure 2). If the reaction proceeds through a transition state having a low ring constraint energy (e.g., seven-membered ring for the 1-6 hydrogen migration reaction), the barrier height is lower than that of a transition state involving a four-membered ring (e.g., 1-3 hydrogen migration). Table 2 shows the barrier heights for three of the isomerization reactions depicted in Figure 2, obtained at the BH&HLYP/cc-pVTZ level of theory.

2.3. Propagation Steps. Besides isomerization, the four initial MB radicals can undergo β -scission reactions. In our previous publication, we identified 13 pathways for the breakdown of MB leading to the formation of small molecules such as CO, H₂CO, CH₃, C₂H₃, and C₂H₄.⁶ The rates for 26 reactions (forward and reverse) are computed using the Rice–Ramsperger–Kassel–Marcus (RRKM) and TST theories with the corrections for hindered rotation and tunneling treatments.

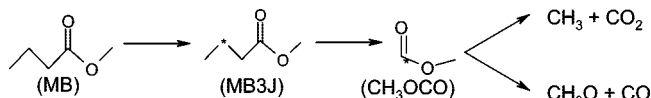


Figure 3. Main reaction pathways for CO₂/CO formation.

A detailed analysis of the reaction pathways identified important pathways for the formation of CO and CO₂. Specifically, radical CH₃CHCH₂C(O)OCH₃ (MB3J), which is formed by H abstraction reaction with an energy barrier of 6.5 kcal/mol, decomposes through a β-scission reaction to form C₃H₆ (propylene) and CH₃OCO. The pathway is reported in Figure 3. Methoxycarbonyl radical, CH₃OCO, is known to be an important intermediate of the reaction of carbon monoxide (CO) with the methoxyl radical (CH₃O).¹² Intermediate CH₃OCO can form CH₃O + CO and CH₃ + CO₂ breaking C–O bonds. The second product channel (CH₃ + CO₂) has a lower barrier of 16.6 kcal/mol as compared to 20.8 kcal/mol to produce CH₃O + CO.

The MB3J radical plays a significant role in the combustion of oxygenated compounds such as alcohol, ether, and ester. Particularly, it has been identified as the main intermediate directly producing CO and CO₂ in the combustion of dimethyl carbonate ((CH₃O)₂CO) in opposed-flow diffusion flames¹³ and in shock tube simulations.¹¹ It is, therefore, crucial to have accurate rate constants for the two following reactions, in order to be able to reproduce the CO₂ concentration profiles correctly.



Reaction R1 is mainly responsible for CO₂ formation while reaction R2 is the main competing reaction in consuming CH₃OCO; thus, it is also important in CO₂ production. The importance of reaction R2 in CO₂ formation is discussed in the section of the sensitivity analysis and rate-of-production analysis.

The rate constants for reaction CH₃ + CO₂ = CH₃OCO (R-1) and CH₃O + CO = CH₃OCO (R-2) were first estimated by Fisher et al.³ based on similarity. In 2005, Glaude et al.¹³ used the transition state theory to calculate the rate constants with the potential energy surface computed at CBS-Q methods. In the study, quantum effects, namely tunneling and recrossing effects, were not included in the calculated rate constants. The rate constants for R1 and R2 were then obtained using thermodynamic properties of the species and TST rate constants of reactions R-1 and R-2, respectively. Using quantum mechanics calculations, McCunn et al.¹² studied the potential energy surface of this reaction, but they did not report explicit values for the rate constants in their study.

Below, we employ high levels of quantum mechanics and direct dynamics methods to study reactions R1 and R2. The new rate constants were included in the MB mechanism to improve the prediction of CO₂ concentration profiles¹¹ and autoignition measurements in shock tube. The updated mechanism was also used to model autoignition data of MB.

3. Computational Details

All of the electronic structure calculations were carried out using the Gaussian 03 program.¹⁴ The G3-method variant (denoted as G3B3)¹⁵ using geometries and zero-point energies obtained from B3LYP density functional theory [B3LYP/6-31G(d)] was used to obtain accurate energetic data for these reactions. The variant is believed to give the energetic information within the chemical accuracy, e.g., 1 kcal/mol. The minimum energy path (MEP) connecting reactant(s) and product(s)

is also obtained at the B3LYP/6-31G(d) level using the intrinsic reaction path (IRC) method. The IRC calculation traces the steepest descent path from the transition state to the corresponding reactant(s) and product(s) using the Gonzalez–Schlegel method¹⁶ with a step size of 0.2 (amu)^{1/2} bohr for a total of 200 steps. The gradient and Hessian for 30 selected points (15 points in each reactant and product channels) along the MEP were obtained at the B3LYP/6-31G(d) level. The selected points along the MEP were chosen using the autofocusing technique,¹⁷ which uses a combination of the barrier shape, and the second derivatives of the Z-matrix geometrical parameters (along the MEP) to predict the regions along the MEP that are sensitive in rate determination.

The rate constants were calculated employing the kinetic module of the web-based computational science and engineering online (CSE-Online) environment.¹⁸ The RRKM theory^{19,20} together with the one-dimensional Eckart methodology^{21,22} is used to calculate rate constants for reactions R1 and R2. Rate constants for the reverse reactions, namely reactions R-1 and R-2, are obtained from those of R1 and R2 and thermodynamic properties of the species (reactant(s) and product(s)). For reaction R2, due to the flat potential energy surface (cf. Figure 6), variational effect is included in the rate constant calculation. A more accurate tunneling correction method such as small curvature tunneling (SCT) correction^{23–25} was also obtained in order to confirm the Eckart tunneling values. Hindered rotation corrections of CH₃ group along the C–O bond (in both CH₃OCO and CH₃–OCO transition state to form CH₃ and CO₂) and CO group along C–O bond (in CH₃O–CO transition state to form CH₃O and CO) are also incorporated in the calculated rate constants using the approach proposed by Ayala and Schlegel.²⁶ This formalism optimizes the accuracy for treating a single rotor to minimize the compound errors in the case of multiple internal rotors. In order to calculate the hindered rotation correction factor for a certain vibrational mode to the partition function, the vibrational mode, the rotating group, as well as the periodicity number of the torsional potential must be identified. From the given information together with the geometry of the interested molecule, information needed for calculating the correction factor of hindered rotation treatment, e.g., reduced moment of inertia and the periodic potential, can be obtained. The correction factor is then calculated using a fitting formula [ref 26 - eq 26] which was derived from the tabulated accurate values to improve upon Pitzer and Gwinn's formula.^{27,28} The fitting formula retains the positive characteristics of Pitzer and Gwinn's formula for high V_0/kT while improving its behavior for low V_0/kT , where V_0 is the internal rotation barrier height.

Discretely calculated values of rate constants for a reaction at different temperatures were fitted to the modified Arrhenius expression as $k(T) = A \times T^n \times \exp(-E_a/RT)$ in the temperature range of 300–2500 K.

4. Results and Discussion

4.1. Rate Constant Calculation. Figure 4 shows the potential energy surface of the decomposition of CH₃OCO to form CH₃ + CO₂ and CH₃O + CO at different levels of theory. CH₃OCO radical has two conformations (*cis* and *trans*) whose energies are very similar with the difference of about 0.3 kcal/mol at G3B3 level. The *trans* conformation can only produce CH₃O + CO with the barrier of 21.5 kcal/mol, while it can decompose to form CH₃ + CO₂ with the barrier of ~33 kcal/mol¹² which is much higher than that from the *cis* configuration

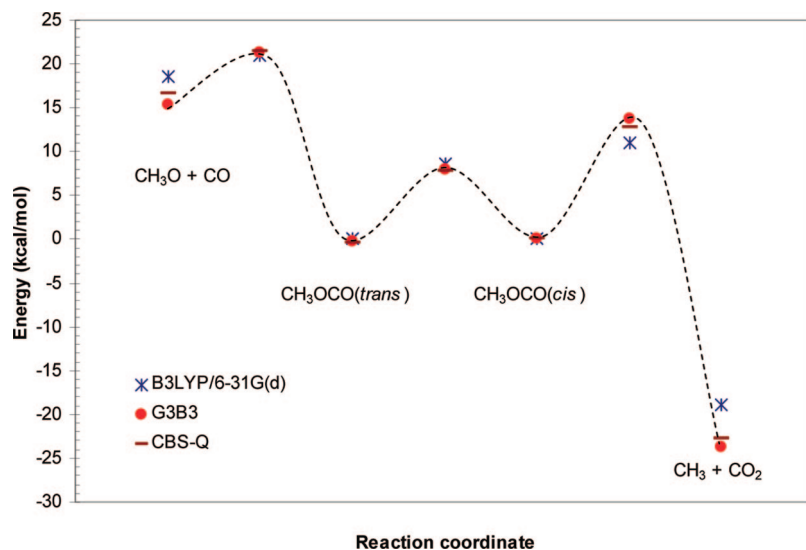


Figure 4. Potential energy surface of the decomposition of CH_3OCO radical. All energy is relative to the energy of the *cis* conformation of CH_3OCO radical, denoted as $\text{CH}_3\text{OCO}(\text{cis})$.

(~ 14 kcal/mol). For this reason, in this study we only consider the *cis* conformation is considered for the $\text{CH}_3 + \text{CO}_2$ channel. Figure 5 shows the geometric parameters for the two conformations of CH_3OCO radical (*cis* and *trans*) as well as the transition state for two decomposition channels at the B3LYP/6-31G(d) level.

It is observed that the barrier height for the isomerization from *cis* to *trans* conformation is significantly lower than those of decomposition channels (7.9 kcal/mol compared to 13.7 and 21.5 kcal/mol for CO_2 and CO channels at G3B3 level, respectively), and the thermodynamic properties ($\Delta H_{f,298K}^\circ$, S , C_p) of these two conformations are very similar. Therefore, only one species name, namely CH_3OCO , is used to represent both conformations in order to simplify the mechanism. This assumption is valid since the inclusion of this isomerization pathway in our mechanism does not affect the results presented in this study.

The potential energy surface for the decomposition of CH_3OCO radical has been calculated by Good and Francisco,²⁹ using the G2 level of theory. The authors recommended the values of 14.7 and 21.8 kcal/mol for the barrier height (ΔV^\ddagger) for reaction R1 and R2, respectively. In 2005, Glaude et al.¹³ used the CBS-Q method to calculate the rate constants and thermodynamic data for related species, reporting barrier heights of 14.7 and 22.7 kcal/mol to CO_2 and CO , respectively. Most recently, using G3B3 level of theory, McCunn et al.¹² computed the value of 13.8 and 21.6 kcal/mol for the barrier height for reaction R1 and R2, respectively. Table 3 lists energetic data for the two reactions R1 and R2.

The latest versions of composite methods such as the G3 method by Curtis et al.¹⁵ and CBS-QB3 method by Peterson and co-workers³⁰ can achieve average accuracies of about 1 kcal/mol when compared to a large set of well-established experimental values; while the early G2 and CBS-Q methods are known to give an accuracy of about 2 kcal/mol. Therefore, the electronic structure calculation results obtained from G3B3, a G3-method variant, are more reliable than those from both G2 and CBS-Q.

In this study, the G3B3 level of theory was used to obtain accurate energetic data for reactions R1 and R2. The B3LYP/6-31G(d) MEP was scaled to obtain the G3B3 vibrationally adiabatic ground-state potential curve $V_{\text{gs}}^{\text{vib}}(s)$, where s is the

reaction coordinate. The reaction coordinate s is defined as the distance along the MEP with the origin located at the saddle point, and it is positive on the product side and negative on the reactant side. The $V_{\text{gs}}^{\text{vib}}(s)$ is the sum of the classical adiabatic ground-state potential curve $V_{\text{e}}(s)$ and the vibrational zero-point energy (VZPE) which was calculated using the B3LYP Hessian data (frequencies) with the scaling factor of 0.96. Figure 6 shows the minimum energy path $V_{\text{gs}}^{\text{vib}}(s)$ for reactions R1 and R2 in the vicinity of the transition states.

4.1.1. Rate Constants for $\text{CH}_3\text{OCO} \rightarrow \text{CH}_3 + \text{CO}_2$ (R1).

Using the G3B3 potential energy surface together with the B3LYP/6-31G(d) gradient, Hessian and geometries, rate constants for the title reaction are computed using different methods with the corrections from tunneling and hindered rotation treatments. Eckart tunneling was included in the RRKM calculation,²¹ while SCT was taken into account for other methods such as canonical variational transition state theory (CVT) and microcanonical variational transition state theory (MVT).^{31,32} The rotation of the CH_3 group along the $\text{C}(\text{H}_3)\text{—O}(\text{CO})$ axis at the reactant and the transition state (cf. Figure 5) was treated as a hindered rotor.

Figure 7 shows the computed rate constants at different temperatures. Since the tunneling factor is close to unity, the tunneling effect is not important for this reaction and decreases with the temperature. For example, the SCT treatment increases the total rate by a factor of 2.2 and 1.08 at 300 and 1000 K, respectively. On the contrary, the correction factor for the hindered rotation (HR) treatment decreases the rate constants noticeably, and the HR effect increases with the temperature. The HR treatment lowers the total rate by a factor of 0.44 and 0.34 at 300 and 1000 K, respectively. It is interesting to find that the three methods, RRKM/Eckart/HR, CVT/SCT/HR, and MVT/SCT/HR, give very similar results in the whole temperature range 300–2500 K (cf. Figure 7). Particularly, the CVT/SCT/HR method gives the middle results between the RRKM/Eckart/HR and MVT/SCT/HR with the maximum difference of 50% in the whole temperature range. The modified Arrhenius expression for the rate constants calculated at the RRKM/Eckart/HR in the temperature range of 300–2500 K is

$$K_{R1}(T) = 1.55 \times 10^{12} \times T^{0.514} \times \exp(-15173/RT),$$

(unit: s⁻¹) (1)

Our calculated rate constants are similar to those proposed by Glaude et al.,¹³ within a difference of 20% for the whole temperature range. Particularly, the new rate constants are 18%

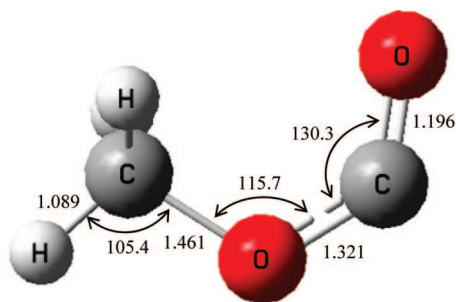
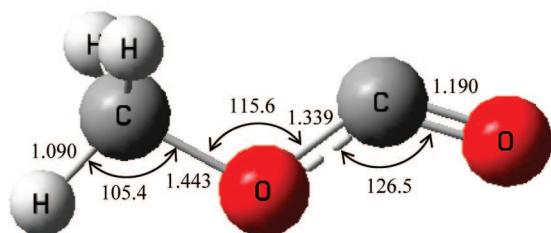
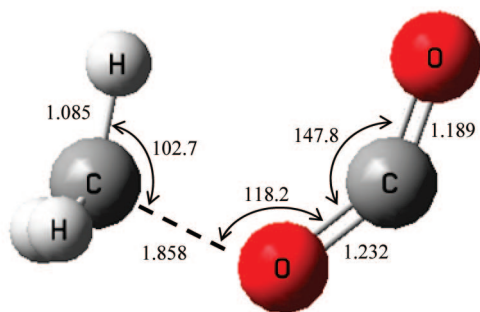
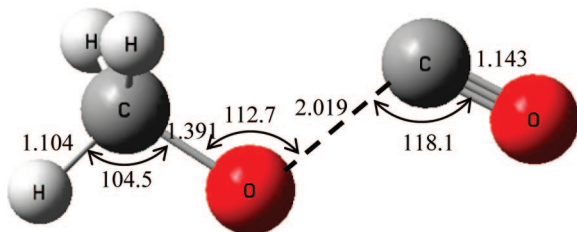
(a) *cis* conformation(b) *trans* conformation(c) Transition state CH₃__CO₂
(from the *cis* conformation)(d) Transition state CH₃O__CO
(from the *trans* conformation)

Figure 5. Optimized geometries for CH₃OCO radical (a) *cis* conformation, (b) *trans* conformations, (c) transition state to CH₃ + CO₂, and (d) transition state to CH₃O + CO. Bond lengths are in angstroms, and angles are in degrees.

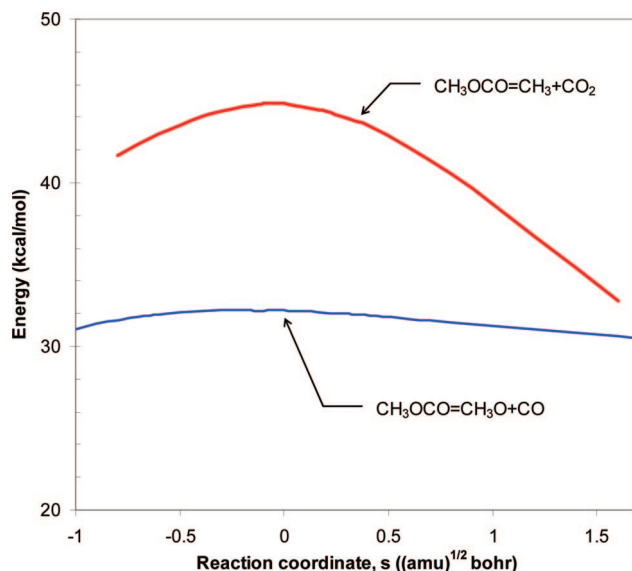


Figure 6. G3B3 minimum energy path in the vicinity of the transition state ($s = 0$) for two channels: CH₃OCO = CH₃ + CO₂ (R1) and CH₃OCO = CH₃O + CO (R2). The energy $V_{\text{g}}^{\text{g}}(s)$ is relative to the classical energy (no zero-point energy correction included) of the reactant, CH₃OCO. CH₃OCO is at $s = -\infty$, while decomposition products (CH₃ + CO₂ and CH₃O + CO for R1 and R2, respectively) are at $s = +\infty$.

TABLE 3: Energetic Information for the Reaction CH₃OCO = CH₃ + CO₂ (R1) and CH₃OCO = CH₃O + CO (R2) at Different Levels of Theory^a

level of theory	ΔV^{\ddagger}	ΔE	$\Delta V_{\text{reverse}}^{\ddagger}$	ref
CH ₃ OCO = CH ₃ + CO ₂ (R1)				
G2	14.7	-21.6	36.3	29
CBS-Q	12.8 (14.7 ^b)	-22.77	35.52	this study
G3B3	13.7	-23.7	37.43	this study (also ref 12)
CH ₃ OCO = CH ₃ O + CO (R2)				
G2	21.8	15.2	6.6	29
CBS-Q	21.8 (22.7 ^b)	17.0	4.8	this study
G3B3	21.5	15.6	5.9	this study (also ref 12)

^a Values are in kcal/mol. ^b The values in parenthesis are from Glaude et al.¹³ using the CBS-Q method.

higher and 14% lower than Glaude's data at 300 and 1500 K, respectively.

4.1.2. Rate Constants for CH₃OCO → CH₃O + CO (R2). Similarly, rate constants for reaction R2 are derived using the G3B3 potential energy surface together with the B3LYP/6-31G(d) gradient, Hessian and geometries. Because the minimum energy path for the CH₃OCO = CH₃O + CO channel in the transition state vicinity is rather "flat" (cf. Figure 6), inclusion of variational effect is expected to give more accurate rate constants for this reaction. Rate constants for this channel were derived using RRKM method with the variational treatment. Corrections from Eckart tunneling and hindered rotation treatments were also included. In addition to the rotation of the CH₃ group along the C(H₃)—O(CO) axis at the reactant and the transition state, the rotation of CO group along the CH₃O—CO axis in the transition state (cf. Figure 5d) is also considered as a hindered rotor.

Similar to reaction R1, the contribution from tunneling treatment is small for the wide temperature range; specifically the tunneling factor is close to unity. While the HR treatment lowers the rate constants of reaction R1, it increases rate

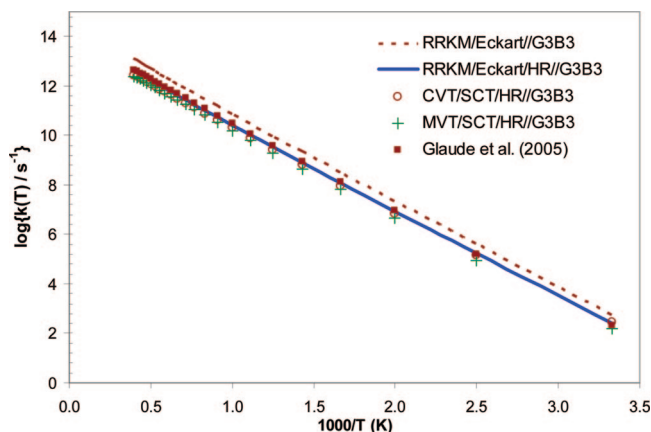


Figure 7. Arrhenius plot of the calculated rate constants and available data from the literature for the $\text{CH}_3\text{OCO} = \text{CH}_3 + \text{CO}_2$ reaction.

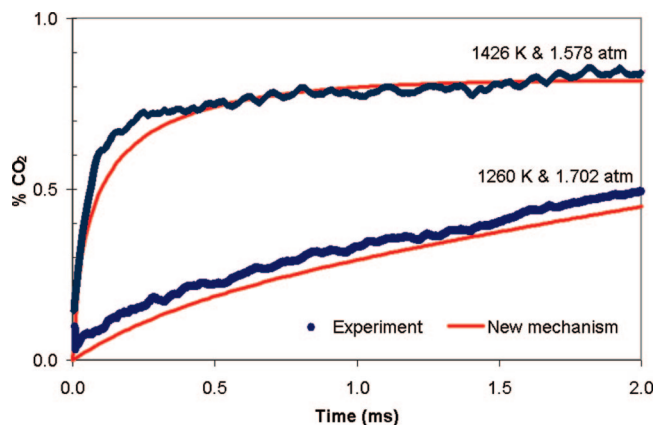


Figure 8. Mole fraction profiles of CO_2 for MB pyrolysis (2% MB in Ar) as a function of time at reflected shock conditions: (a) $T = 1260$ K and $P = 1.702$ atm and (b) $T = 1426$ K and $P = 1.578$ atm.

TABLE 4: Main Reactions for the Formation of CO_2 during MB Pyrolysis^a

reactions	no.
$\text{CH}_3\text{OCO} = \text{CH}_3 + \text{CO}_2$	(R1)
$\text{CH}_3\text{OCO} = \text{CH}_3\text{O} + \text{CO}$	(R2)
$\text{CH}_3\text{CH}_2\text{CH}_2\text{COO}(\text{BAOJ}) + \text{CH}_3 = \text{MB}$	(R3)
$\text{MB} + \text{H} = \text{CH}_3\text{CHCH}_2\text{COOCH}_3(\text{MB3J}) + \text{H}_2$	(R4)
$\text{CH}_3\text{CHCH}_2\text{COOCH}_3(\text{MB3J}) = \text{CH}_3\text{OCO} + \text{C}_3\text{H}_6$	(R5)
$\text{MB} + \text{H} = \text{CH}_2\text{CH}_2\text{CH}_2\text{COOCH}_3(\text{MB4J}) + \text{H}_2$	(R6)
$\text{CH}_2\text{CO}_2\text{CH}_3 + \text{C}_2\text{H}_5 = \text{MB}$	(R7)
$\text{CH}_3\text{CH}_2\text{CH}_2\text{COO}(\text{BAOJ}) = n\text{-C}_3\text{H}_7 + \text{CO}_2$	(R8)
$\text{MB} = n\text{-C}_3\text{H}_7 + \text{CH}_3\text{OCO}$	(R9)
$\text{MB} = \text{CH}_3 + \text{CH}_2\text{CH}_2\text{COOCH}_3(\text{MP3J})$	(R10)
$\text{CH}_2\text{CH}_2\text{COOCH}_3(\text{MP3J}) = \text{C}_2\text{H}_4 + \text{CH}_3\text{OCO}$	(R11)
$\text{MB} + \text{H} = \text{CH}_3\text{CH}_2\text{CH}_2\text{COOCH}_2(\text{MBMJ}) + \text{H}_2$	(R12)
$\text{CH}_3\text{CH}_2\text{CH}_2\text{COOCH}_2(\text{MBMJ}) = \text{CH}_3\text{CHCH}_2\text{COOCH}_3(\text{MB3J})$	(R13)

^a Abbreviations used by Fisher et al.⁴ for selected MB-related radical species are given in parentheses.

constants of reaction R2 with temperature. For example, the rate constants are 2.4 and 2.7 times faster at 1000 and 1500 K, respectively. This rate constant increase can be explained by the HR treatment of the rotation of CO group along the $\text{CH}_3\text{O}-\text{CO}$ axis in the transition state which is not treated as a hindered rotor in reaction R1. The variational effect is found to be more important for this reaction than for reaction R1 due to the “flat” potential energy surface. For example, the variational treatment lowers the rate by a factor of 2.4 and 2.1 at 1000 and 1500 K, respectively. The modified Arrhenius expression for

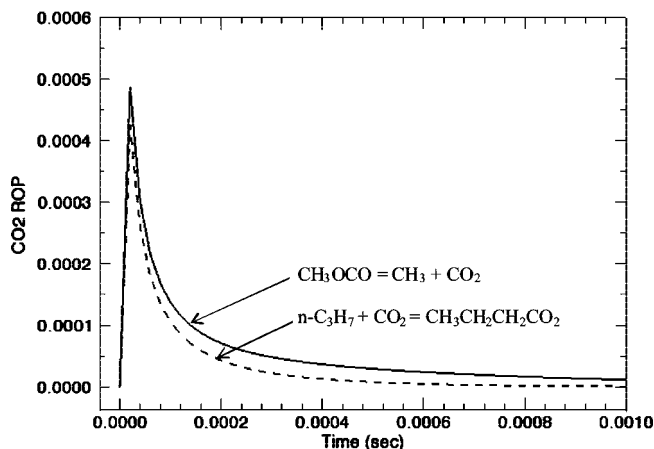


Figure 9. Rate-of-production (ROP) for CO_2 as a function of time at initial conditions of 1426 K, 1.58 atm, and 2% MB in argon for the two most important reactions in the CO_2 formation.

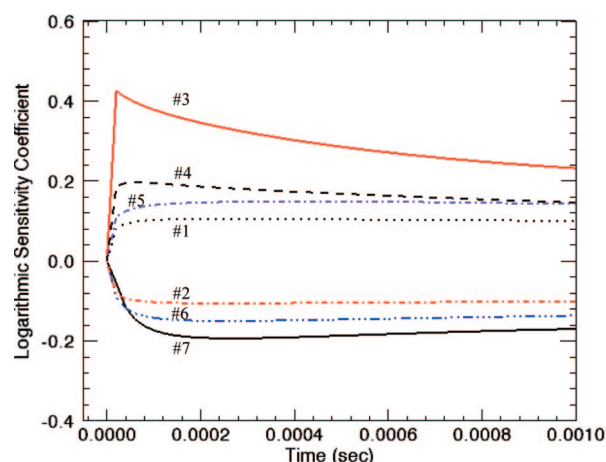


Figure 10. Sensitivity analysis for CO_2 as a function of time at initial conditions of 1426 K, 1.58 atm, 2% MB in argon. The seven largest sensitivity coefficients are shown.

the rate constants calculated in the temperature range of 300–2500 K is

$$K_{R2}(T) = 7.37 \times 10^{12} \times T^{0.479} \times \exp(-23792/RT),$$

(unit: s^{-1}) (2)

By effectively varying the dividing surface along the MEP between the reactants and products, variational treatment minimizes the recrossing effects, lowering the calculated rate constant, e.g., TST rate constant. Our rate constants for reaction R2 are found 4 times lower than those introduced by Glaude et al. at 1500 K. Considering the smaller difference in the rate constants for R1 compared with R2, the difference in the latter is responsible for the higher CO_2/CO branching ratio compared to that proposed by Glaude et al.

4.1.3. Rate Constants for $\text{CH}_3 + \text{CO}_2 \rightarrow \text{CH}_3\text{OCO}$ (R-1) and $\text{CH}_3\text{O} + \text{CO} \rightarrow \text{CH}_3\text{OCO}$ (R-2). With the use of thermodynamic properties of related species calculated at G3B3 level of theory and the calculated rate constants for reactions R1 and R2, rate constants for reverse reactions R-1 and R-2 can be accurately derived, respectively. The rate constants for reaction R-1 and R-2 can be expressed using the modified Arrhenius form as

$$k_{R-1}(T) = 6.89 \times 10^6 T^{1.774} \exp(-18459/RT),$$

(unit: $\text{cm}^3 \text{mol}^{-1} \text{s}^{-1}$) (3)

$$k_{R-2}(T) = 7.10 \times 10^5 T^{1.897} \exp(-3356/RT),$$

(unit: $\text{cm}^3 \text{mol}^{-1} \text{s}^{-1}$) (4)

4.2. New Kinetic Mechanism for Methyl Butanoate. The new pathways and reaction rates for MB decomposition were embedded into the latest version of the chemical model presented

by Fisher et al.³ (version 2004 obtained at <http://www-cmls.llnl.gov/> composed of 264 species and 1219 reactions.

In addition to the simple unimolecular decomposition (one bond breaking at a time), the six-centered unimolecular elimination reaction (multiple bonds breaking and forming at the same time) yielding ethylene and methyl acetate^{5,9} was included in

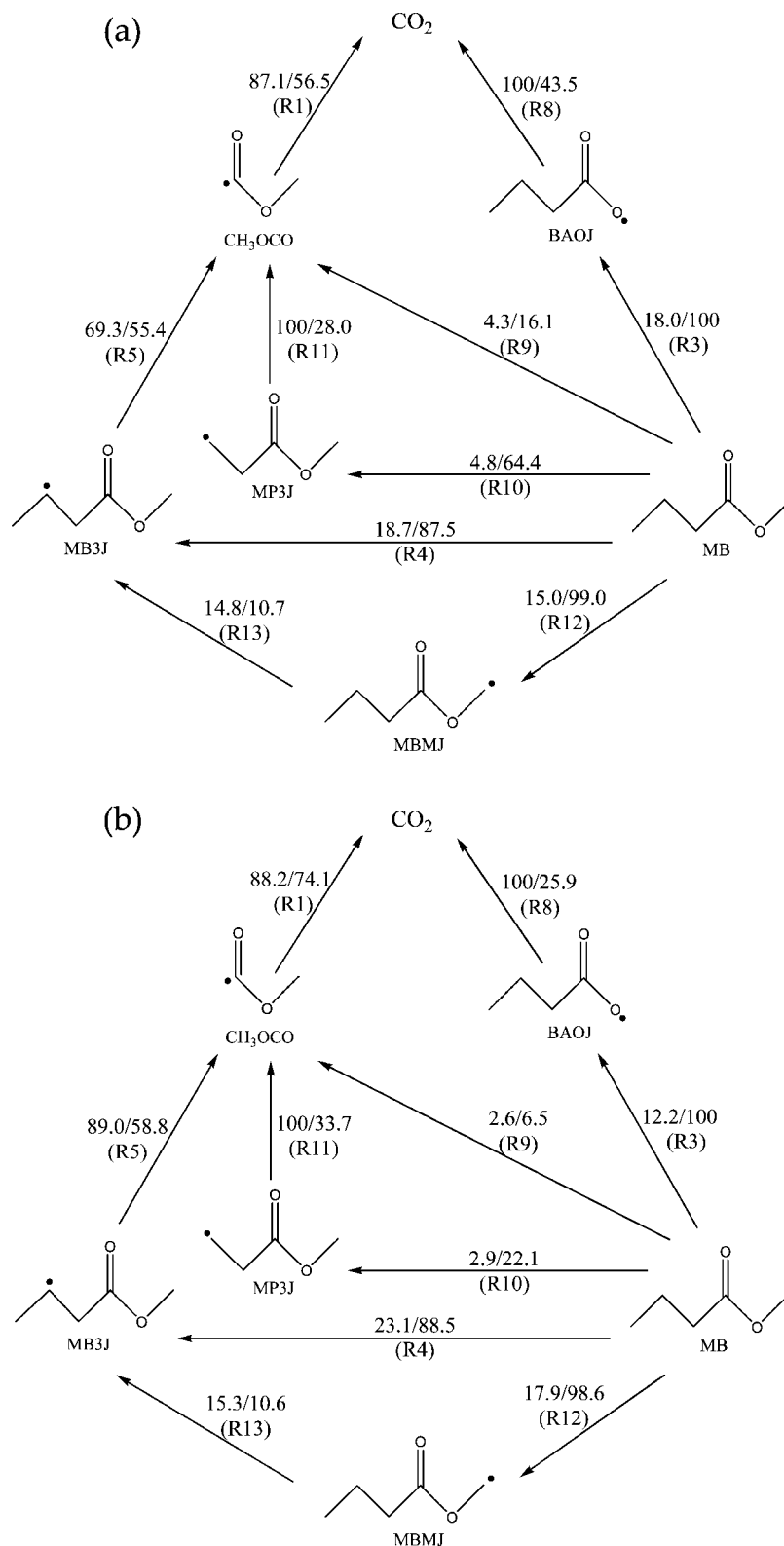


Figure 11. Flux analyses for the formation of CO_2 during the MB pyrolysis at $T = 1426$ K and $P = 1.578$ atm in the shock tube. The analysis was carried out with the new kinetic mechanism at different residence times: (a) $\tau = 0.1$ ms and (b) $\tau = 0.4$ ms. The most important reactions involved in each pathway are given in parentheses. The notation “A/B” means A% reactant produces B% product in the considered channel.

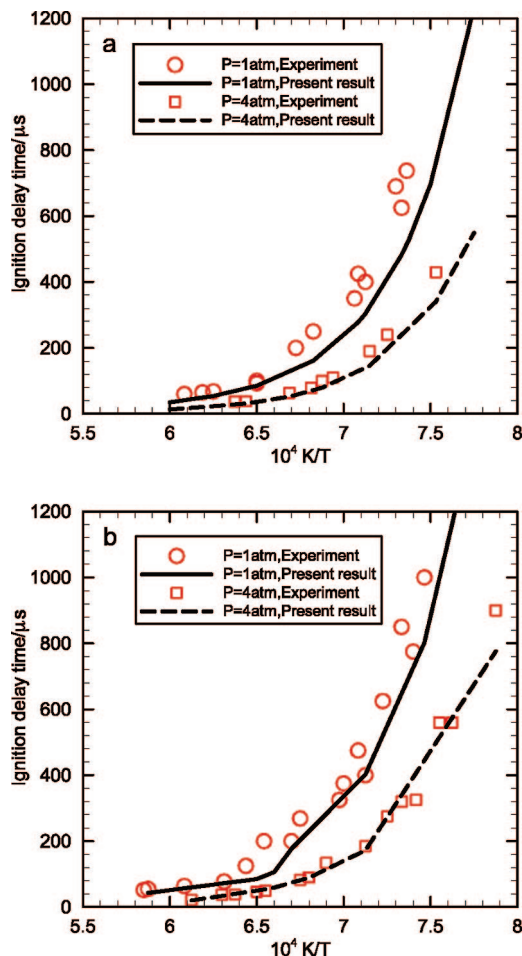


Figure 12. Calculated and measured ignition delay times of MB/O₂/Ar mixtures versus temperature for pressures of 1 and 4 atm at (a) equivalence ratio $\phi = 1$ and (b) equivalence ratio $\phi = 1.5$. Experimental data were taken from ref 8.

the mechanism. This pathway requires the inclusion of the methyl acetate decomposition submodel suggested by Westbrook and co-workers¹⁰ in the kinetic mechanism.

The final kinetic model and associated thermochemistry will be available for download from the Web site of Prof. Violi at <http://www-personal.umich.edu/~avioli/mechs.html>.

4.3. CO₂ Prediction in Shock Tube Simulation. The new MB mechanism is used to study the formation of CO₂ in a shock tube. The “Reflected Shock Reactor” module of the Chemkin 4.1 package³³ is used to simulate the experiments. Shock tube simulations are zero-dimensional and begin at the onset of the reflected shock period assuming constant volume and homogeneous adiabatic conditions behind the reflected shock wave.

The experimental data have been recently obtained by the research group of Prof. Hanson at Stanford.¹¹ The reactor is fed with 2% MB in Ar, and two conditions were analyzed: (i) $T = 1260$ K and $P = 1.702$ atm and (ii) $T = 1426$ K and $P = 1.578$ atm. The comparison between the experimental data and the computed results for the concentration of CO₂ is reported in Figure 8.

The newly assembled kinetic model gives a very good agreement with the experimental CO₂ profiles for the two cases. The error is within 10% of the experimental data for the whole residence time. The concentration of CO₂ is controlled by both reactions R1 and R2, where reaction R1 is mainly responsible for CO₂ formation while reaction R2 is the main competing reaction of consuming CH₃OCO radical. Using the new MB

model, rate-of-production (ROP) and sensitivity analyses for CO₂ formation were performed at the reflected shock tube conditions of 1426 K and 1.58 atm. Table 4 lists the main reactions involved in the formation of CO₂ for the shock tube simulations.

The ROP for CO₂ at 1426 K and 1.58 atm is presented in Figure 9 for the residence time τ between 0 and 1 ms. The two dominant pathways for the formation of CO₂ are the breaking of the C—O bond, via the decomposition of CH₃OCO (reaction R1) and CH₃CH₂CH₂COO (reaction R8). The two reactions contribute evenly to the formation of CO₂ for the first ~ 0.05 ms; after that the contribution of R1 becomes slightly predominant.

Figure 10 shows the seven largest sensitivity coefficients at 1426 K and 1.58 atm. The sensitivity analysis supports the ROP interpretation. The concentration of CO₂ is strongly influenced by the initial decomposition pathways of MB through reaction R3 leading to the formation of CH₃CH₂CH₂COO (BAOJ) and then CO₂ via R8 and to a less extent by reaction R7, whose product, CH₃CO₂CH₃, decomposes to form two separate oxygen-carrying moieties leading to the formation of CO. This explains the negative sensitivity values for reaction R7. The CO₂ concentration is also relatively sensitive to two of the MB + H hydrogen abstraction reactions, R4 and R6. The product of reaction R4, CH₃CHCH₂COOCH₃ (MB3J), breaks into C₃H₆ and CH₃OCO, which can form CO₂ through reactions R5. CH₂CH₂CH₂COOCH₃ (MB4J), a product from reaction R6, eventually produces CO through the CH₂COOCH₃ formation by the β -scission reaction (not given in Table 4). This explains the sign of the sensitivity coefficients for these reactions. In other words, the increase of the rate constants for reaction R4 (positive values) and R6 (negative values) will increase and decrease the CO₂ concentration, respectively. CH₃OCO can decompose to form either CO₂ or CO by reactions R1 and R2, respectively.

To understand further the formation of CO₂ during the MB breakdown, flux analyses were carried out using the new kinetic mechanism. Figure 11 shows the flux analyses for CO₂ formation in the shock tube ($T = 1426$ K and $P = 1.578$ atm) at a residence time of 0.1 ms (Figure 11a) and 0.4 ms (Figure 11b). In both cases, CO₂ is produced by two main pathways involving β -scission reactions.

At $\tau = 0.1$ ms, 87.1% CH₃OCO (through reaction R1) and 100% BAOJ (through reaction R8) are responsible for 56.5% and 43.5% CO₂ formation, respectively.

As the simulation proceeds, the CH₃OCO channel becomes more important, accounting for 74.1% of CO₂ formation compared to 25.9% for the BAOJ channel at $\tau = 0.4$ ms. CH₃OCO can be formed from MB directly through the unimolecular decomposition reaction (reaction R9) or indirectly through the hydrogen abstraction reactions to create MB3J and MP3J (reactions R4 and R10, respectively) and the combination between hydrogen abstraction and hydrogen migration from MBMJ (reaction R12 and R13). Note that CH₃OCO can directly dissociate to both CO₂ and CO at the same time, thus reactions R1 and R2 are important in CO₂ formation as presented in the sensitivity analysis (cf. Figure 10). For convenience in discussion, the net flux ratio between the two channels from CH₃OCH to CO₂ and CO can be denoted as (CH₃OCO \rightarrow CO₂) and (CH₃OCO \rightarrow CO), respectively. The net flux is the product (sum) of the forward and reverse flux for each channel. As the time elapses, the CO₂ dissociation channel becomes more and more important; particularly, the (CH₃OCO \rightarrow CO₂)/(CH₃OCO \rightarrow CO) ratio is 6.7 and 7.4 at $\tau = 0.1$ and $\tau = 0.4$ ms, respectively.

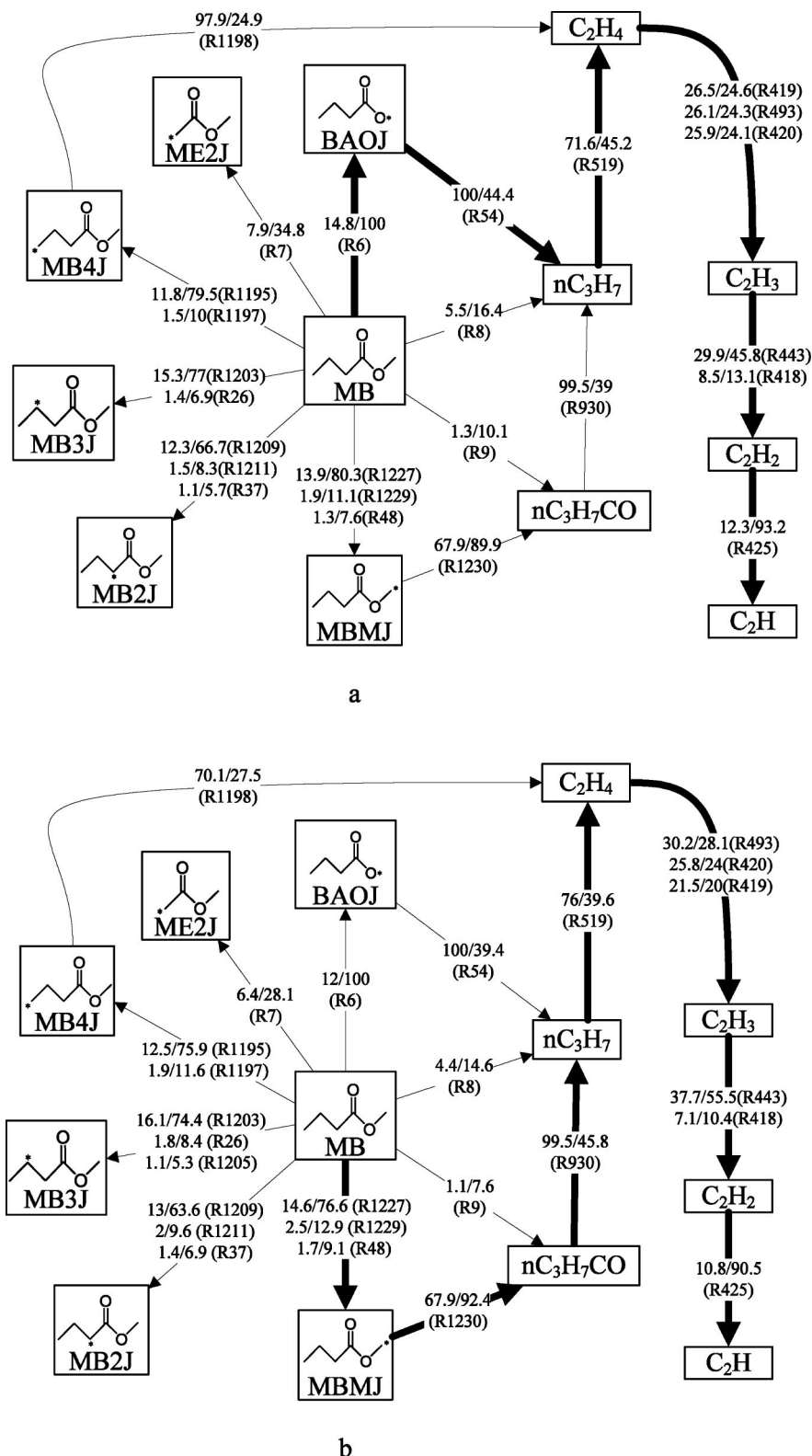


Figure 13. Flux analysis for the most important C₂H formation pathways and primary alkyl radical formation at $\phi = 1$ and two pressures: (a) 1 atm and (b) 4 atm. The notation “A/B” means A% reactant produces B% product in the considered channel; the reaction numbers are from the final MB kinetic mechanism.

The barrier height for the reaction $\text{CH}_3\text{OCO} = \text{CH}_3 + \text{CO}_2$ (R1) is lower than that of $\text{CH}_3\text{OCO} = \text{CH}_3\text{O} + \text{CO}$ (R2) by ~ 7.5 kcal/mol (cf. Table 3); thus in terms of chemical kinetics, rate constants of the latter reaction become comparable to those of the former at high temperatures. Note that in the shock tube reactor, the temperature decreases from the reflected shock temperature as the process proceeds due to the energy absorption

in breaking chemical bonds. As temperature decreases reaction R1 to dominate over R2. This explains the increase trend of the $(\text{CH}_3\text{OCO} \rightarrow \text{CO}_2)/(\text{CH}_3\text{OCO} \rightarrow \text{CO})$ ratio with the residence time.

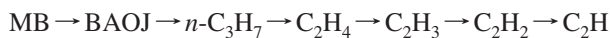
4.4. MB Ignition Delay Times in Shock Tube. In order to provide more information on the combustion characteristics of MB and to extend the range of applicability of the new kinetic

mechanism, we carried out simulations of shock tube ignition delay times for MB. The experimental data were taken from Dooley et al.⁸ The numerical simulations were performed using MB/O₂/Ar mixtures over the temperature range 1295–1632 K at reflected shock pressures of 1.0 and 4.0 atm and equivalence ratios of 1 and 1.5. We defined the ignition delay time as the time at which the maximum value of $[\dot{\text{C}}_2\text{H}] \times [\dot{\text{O}}]$ occurs.³⁵ Figure 12 presents the results of calculated ignition delay times of MB/O₂/Ar mixtures at different temperatures, pressures, and equivalence ratios, together with the experimental data from the literature.⁸ The MB/O₂/Ar mixtures in the shock tube contain 1% MB, 13% O₂, and 86% Ar for an equivalence ratio of 1 and 1.5% MB, 6.5% O₂, and 92% Ar for an equivalence ratio of 1.5. The kinetic mechanism correctly reproduces the experimental data as function of the temperature, pressure, and equivalence ratios.

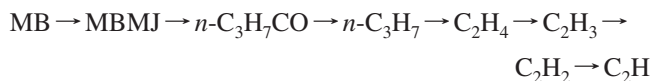
To analyze the important channels that determine the ignition delay times in different conditions, a detailed analysis of the rates of production for net and major reaction pathways for O and C₂H was carried out. Reactions $\text{H} + \text{O}_2 = \text{OH} + \text{O}$ and $\text{C}_2\text{H}_2 + \text{OH} = \text{C}_2\text{H} + \text{H}_2\text{O}$ are the dominant reactions for the formation of O and C₂H radicals, respectively.

Figure 13 shows the reaction pathways for the formation of C₂H and primary alkyl radicals at an equivalence ratio of 1 and pressures equal to 1 atm (Figure 13a) and 4 atm (Figure 13b).

The reaction pathways were extracted at 50% MB consumption. In Figure 13a, the pressure of 1 atm corresponds to a time of 8 μs and a temperature of 1475 K with a simulated ignition delay of 100 μs . The main pathways contributing to the formation of C₂H are



Produced from MB by C–O bond scission through reaction R-6, BAOJ undergoes β scission to form $n\text{-C}_3\text{H}_7$ that further reacts to form ethane. Ethane subsequently decomposes via a series of hydrogen abstraction reactions to yield C₂H. The fuel radical formed in the largest quantity is MBMJ (17%), which also contributes to the formation of C₂H. The other two most abundant radicals are MB3J and MB2J. In Figure 13b, the pressure of 4 atm corresponds to a time of 6 μs and a temperature of 1480 K with a simulated ignition delay of 40 μs . As the pressure increases, the presence of MB3J among the fuel radicals becomes significant reaching 19%, followed by MBMJ with 18.8%, and MB2J with 16.4%. The main pathways of for the formation of C₂H are



MBMJ (18.8%) leads to the formation of ethene via a series of C–O and C–C bond breaking, and finally the C₂H radical is produced via hydrogen abstraction reactions.

5. Conclusions

This paper reports on new reaction pathways for the breakdown of methyl butanoate obtained using quantum mechanics and direct dynamics methods. The pathways and the reaction rates were computed using ab initio methods. This submechanism is coupled to the kinetic mechanism reported by Fisher et al. [*Proc. Combust. Inst.* **2000**, 28, 1579] together with the addition of the six-centered unimolecular elimination reaction that yields ethylene and methyl acetate and the inclusion of the methyl acetate decomposition model. This new mechanism is then used to predict the mole fractions of CO₂ in shock

tube experiments available in the literature. The capability of CO₂ prediction was improved by obtaining accurate rate constants for reactions $\text{CH}_3\text{OCO} = \text{CH}_3 + \text{CO}_2$ and $\text{CH}_3\text{OCO} = \text{CH}_3\text{O} + \text{CO}$ using the Rice–Ramsperger–Kassel–Marcus theory with corrections from tunneling, hindered rotation, and variational treatments.

The computed CO₂ concentration profiles are in very good agreement with the experimental data. Rate-of-production and sensitivity analyses are carried out for the new mechanism, and other kinetics available in the literature to investigate the pathways for the formation of CO₂ during the MB breakdown.

The MB mechanism was also used to simulate ignition delay times in the shock tube. Under the effect of temperature, pressure, and equivalence ratio, the results of simulation are consistent with experimental data. Reactions $\text{H} + \text{O}_2 = \text{OH} + \text{O}$ and $\text{C}_2\text{H}_2 + \text{OH} = \text{C}_2\text{H} + \text{H}_2\text{O}$ are found to be the dominant reactions for the formation of O and C₂H radicals, respectively. In addition, the pressure (in the correlation with temperature) affects the variation of predominant reaction pathways for the C₂H radical and primary alkyl radical formed from MB.

The new MB mechanism is able to correctly predict the concentration profiles of CO₂ in pyrolysis conditions as well as ignition delay time in oxidation conditions, thus giving a better chemical insight of combustion/pyrolysis of MB. Such results are encouraging, and this mechanism can be used as a basis for future implementations of the kinetics of biodiesel esters.

Acknowledgment. This research is funded in part by the U.S. Air Force Scientific Office for Research (Grant FA9550-06-1-0376). The authors are grateful to Prof. R. Hanson for the data on shock tube experiments, to Dr. C. Westbrook for providing the kinetic mechanism for alkyl esters, and to Dr. H.-H. Carstensen for discussion on calculation of thermodynamic properties.

References and Notes

- (1) Graboski, M. S.; McCormick, R. L. *Prog. Energy Combust. Sci.* **1998**, 24, 125.
- (2) Hill, J.; Nelson, E.; Tilman, D.; Polasky, S.; Tiffany, D. *Proc. Natl. Acad. Sci. U.S.A.* **2006**, 103, 11206.
- (3) Fisher, E. M.; Pitz, W. J.; Curran, H. J.; Westbrook, C. K. *Proc. Combust. Inst.* **2000**, 28, 1579.
- (4) Gail, S.; Thomson, M. J.; Sarathy, S. M.; Syed, S. A.; P. Dagaut; Dievart, P.; Marchese, A. J.; Dryer, F. L. *Proc. Combust. Inst.* **2007**, 31, 305.
- (5) Metcalfe, W. K.; Dooley, S.; Curran, H. J.; Simmie, J. M.; Al-Nahas, A. M.; Navarro, M. V. *J. Phys. Chem. A* **2007**, 111, 4001.
- (6) Huynh, L. K.; Violi, A. J. *Org. Chem.* **2008**, 73, 94.
- (7) Westbrook, C. K.; Pitz, W. J.; Curran, H. J. *J. Phys. Chem. A* **2006**, 110, 6912.
- (8) Dooley, S.; Curran, H. J.; Simmie, J. M. *Combust. Flame* **2008**, 153, 2.
- (9) El-Nahas, A. M.; Navarro, M. V.; Simmie, J. M.; Joseph, W.; Bozzelli; Curran, H. J.; Dooley, S.; Metcalfe, W. *J. Phys. Chem. A* **2007**, 111, 3727.
- (10) Westbrook, C. K.; Pitz, W. J.; Westmoreland, P. R.; Dryer, F. L.; Chaos, M.; Osswald, P.; Kohse-Hoinghaus, K.; Cool, T. A.; Wang, J.; Yang, B.; Hansen, N.; Kasper, T. *Proc. Combust. Inst.* Accepted.
- (11) Farooq, A.; Davidson, D. F.; Hanson, R. K.; Huynh, L. K.; Violi, A. *Proc. Combust. Inst.* Accepted.
- (12) McCunn, L. R.; Lau, K.-C.; Krisch, M. J.; Butler, L. J.; Tsung, J.-W.; Lin, J. J. *J. Phys. Chem. A* **2006**, 110, 1625.
- (13) Glaude, P. A.; Pitz, W. J.; Thomson, M. J. *Proc. Combust. Inst.* **2005**, 30, 1111.
- (14) Frisch, M. J.; Trucks, G. W.; Schlegel, H. B.; Scuseria, G. E.; Robb, M. A.; Cheeseman, J. R.; Montgomery, J. A., Jr.; Vreven, T.; Kudin, K. N.; Burant, J. C.; Millam, J. M.; Iyengar, S. S.; Tomasi, J.; Barone, V.; Mennucci, B.; Cossi, M.; Scalmani, G.; Rega, N.; Petersson, G. A.; Nakatsuji, H.; Hada, M.; Ehara, M.; Toyota, K.; Fukuda, R.; Hasegawa, J.; Ishida, M.; Nakajima, T.; Honda, Y.; Kitao, O.; Nakai, H.; Klene, M.; Li, X.; Knox, J. E.; Hratchian, H. P.; Cross, J. B.; Adamo, C.; Jaramillo, J.; Gomperts, R.; Stratmann, R. E.; Yazyev, O.; Austin, A. J.; Cammi, R.;

Pomelli, C.; Ochterski, J. W.; Ayala, P. Y.; Morokuma, K.; Voth, G. A.; Salvador, P.; Dannenberg, J. J.; Zakrzewski, V. G.; Dapprich, S.; Daniels, A. D.; Strain, M. C.; Farkas, O.; Malick, D. K.; Rabuck, A. D.; Raghavachari, K.; Foresman, J. B.; Ortiz, J. V.; Cui, Q.; Baboul, A. G.; Clifford, S.; Cioslowski, J.; Stefanov, B. B.; Liu, G.; Liashenko, A.; Piskorz, P.; Komaromi, I.; Martin, R. L.; Fox, D. J.; Keith, T.; Al-Laham, M. A.; Peng, C. Y.; Nanayakkara, A.; Challacombe, M.; Gill, P. M. W.; Johnson, B.; Chen, W.; Wong, M. W.; Gonzalez, C.; Pople, J. A. GAUSSIAN03. In *Gaussian 03, Revision A.1*; Gaussian, Inc.: Pittsburgh, PA, 2003.

(15) Baboul, A. G.; Curtiss, L. A.; Redfern, P. C.; Raghavachari, K. *J. Chem. Phys.* **1999**, *110*, 7650.

(16) Gonzalez, C.; Schlegel, H. B. *J. Phys. Chem.* **1990**, *94*, 5523.

(17) Duncan, W. T.; Bell, R. L.; Truong, T. N. *J. Comput. Chem.* **1998**, *19*, 1039.

(18) Truong, T. N.; Nayak, M.; Huynh, H. H.; Cook, T.; Mahajan, P.; Tran, L.-T. T.; Bharath, J.; Jain, S.; Pham, H. B.; Boonyasiriwat, C.; Nguyen, N.; Eren, E.; Kim, Y.; Choe, S.; Choi, J.; Cheatham, T. E., III.; Facelli, J. C. *J. Chem. Inf. Model.* **2006**, *46*, 971.

(19) Forst, W. *Theory of Unimolecular Reactions*; Academic Press: New York, 1973.

(20) Gilbert, R. G.; Smith, S. C. *Theory of Unimolecular and Recombination Reactions*; Blackwell: Oxford, 1990.

(21) Zhang, S.; Truong, T. N. *J. Phys. Chem. A* **2001**, *105*, 2427.

(22) Miller, W. H. *J. Am. Chem. Soc.* **1979**, *101*, 6810.

(23) Truhlar, D. G.; Garrett, B. C. *Acc. Chem. Res.* **1980**, *13*, 440.

(24) Truhlar, D. G.; Isaacson, A. D.; Garrett, B. C. *Theory of Chemical Reaction Dynamics*; Baer, M., Ed.; CRC Press: Boca Raton, FL, 1985; Vol. 4; p 65.

(25) Truong, T. N.; Truhlar, D. G. *J. Chem. Phys.* **1990**, *93*, 1761.

(26) Ayala, P. Y.; Schlegel, H. B. *J. Chem. Phys.* **1998**, *108*, 2314.

(27) Pitzer, K. S.; Gwinn, W. D. *J. Chem. Phys.* **1942**, *10*, 428.

(28) Li, J. C. M.; Pitzer, K. S. *J. Phys. Chem.* **1956**, *60*, 466.

(29) Good, D. A.; Francisco, J. S. *J. Phys. Chem. A* **2000**, *104*, 1171.

(30) Montgomery, J. A., Jr.; Frisch, M. J.; Ochterski, J. W. *J. Chem. Phys.* **2000**, *112*, 6532.

(31) Truhlar, D. G.; Isaacson, A. D.; Garrett, B. C. Generalized Transition State Theory. In *Theory of Chemical Reaction Dynamics*; Baer, M., Ed.; CRC Press: Boca Raton, FL, 1985; Vol. 4; pp 65.

(32) Truhlar, D. G. Direct Dynamics Method for the Calculation of Reaction Rates In *The Reaction Path in Chemistry: Current Approaches and Perspectives*; Heidrich, D., Ed.; Kluwer Academic: Dordrecht, 1995; pp 229.

(33) Kee, R. J.; Rupley, F. M.; Miller, J. A.; Coltrin, M. E.; Grcar, J. F.; Meeks, E.; Moffat, H. K.; Lutz, A. E.; Dixon-Lewis, G.; Smooke, M. D.; Warnatz, J.; Evans, G. H.; Larson, R. S.; Mitchell, R. E.; Petzold, L. R.; Reynolds, W. C.; Caracotsios, M.; Stewart, W. E.; Glarborg, P.; Wang, C.; McLellan, C. L.; Adigun, O.; Houf, W. G.; Chou, C. P.; Miller, S. F.; Ho, P.; Young, P. D.; Young, D. J.; Hodgson, D. W.; Petrova, M. V.; Pudukkham, K. V. *CHEMKIN Release 4.1*; Reaction Design: San Diego, CA, 2006.

(34) Dagaut, P. *Phys. Chem. Chem. Phys.* **2002**, *4*, 1846.

(35) Grebe, J.; Homann, K. H. *Ber. Bunsen-Ges. Phys. Chem.* **1982**, *86*, 597.

JP804358R